

UC Davis

UC Davis Previously Published Works

Title

Microtubule-associated protein IQ67 DOMAIN5 regulates morphogenesis of leaf pavement cells in *Arabidopsis thaliana*.

Permalink

<https://escholarship.org/uc/item/95k6b7n0>

Journal

Journal of Experimental Botany, 70(2)

Authors

Mitra, Dipannita
Klemm, Sandra
Kumari, Pratibha
[et al.](#)

Publication Date

2019-01-07

DOI

10.1093/jxb/ery395

Peer reviewed



RESEARCH PAPER

Microtubule-associated protein IQ67 DOMAIN5 regulates morphogenesis of leaf pavement cells in *Arabidopsis thaliana*

Dipannita Mitra^{1,*}, Sandra Klemm^{1,*}, Pratibha Kumari^{1,*}, Jakob Quegwer¹, Birgit Möller^{2,◊}, Yvonne Poeschl^{2,3,◊}, Paul Pflug¹, Gina Stamm¹, Steffen Abel^{1,4,5,◊} and Katharina Bürstenbinder^{1,†,◊}

¹ Department of Molecular Signal Processing, Leibniz Institute of Plant Biochemistry (IPB), D-06120 Halle (Saale), Germany

² Institute of Computer Science, Martin Luther University Halle-Wittenberg, D-06120 Halle (Saale), Germany

³ iDiv, German Integrative Research Center for Biodiversity, D-04103 Leipzig, Germany

⁴ Institute of Biochemistry and Biotechnology, Martin Luther University Halle-Wittenberg, D-06120 Halle (Saale), Germany

⁵ Department of Plant Sciences, University of California, Davis, CA 95616, USA

* These authors contributed equally to this work.

† Correspondence: Katharina.Buerstenbinder@ipb-halle.de

Received 3 August 2018; Editorial decision 16 October 2018; Accepted 22 November 2018

Editor: Simon Turner, University of Manchester, UK

Abstract

Plant microtubules form a highly dynamic intracellular network with important roles for regulating cell division, cell proliferation, and cell morphology. Their organization and dynamics are co-ordinated by various microtubule-associated proteins (MAPs) that integrate environmental and developmental stimuli to fine-tune and adjust cytoskeletal arrays. IQ67 DOMAIN (IQD) proteins recently emerged as a class of plant-specific MAPs with largely unknown functions. Here, using a reverse genetics approach, we characterize *Arabidopsis* IQD5 in terms of its expression domains, subcellular localization, and biological functions. We show that IQD5 is expressed mostly in vegetative tissues, where it localizes to cortical microtubule arrays. Our phenotypic analysis of *iqd5* loss-of-function lines reveals functions of IQD5 in pavement cell (PC) shape morphogenesis. Histochemical analysis of cell wall composition further suggests reduced rates of cellulose deposition in anticlinal cell walls, which correlate with reduced anisotropic expansion. Lastly, we demonstrate IQD5-dependent recruitment of calmodulin calcium sensors to cortical microtubule arrays and provide first evidence for important roles for calcium in regulation of PC morphogenesis. Our work identifies IQD5 as a novel player in PC shape regulation and, for the first time, links calcium signaling to developmental processes that regulate anisotropic growth in PCs.

Keywords: *Arabidopsis*, calcium, calmodulin, cell wall, IQ67 DOMAIN, microtubules, pavement cell shape, signaling

Introduction

The plant cytoskeleton, comprised of actin filaments and microtubules (MTs), forms a three-dimensional intracellular network that determines cell division and cell morphology, and serves as tracks for cellular transport of various cargoes, including organelles, proteins, and other macromolecular complexes (Wasteneys and Yang, 2004b; Hussey *et al.*, 2006; Akhmanova

and Hammer, 2010). Networks of MTs form highly dynamic arrays and adopt specific functions during the plant life cycle, including essential roles in cell division and expansion, intra- and intercellular transport, cellular organization, and the deposition of cell wall material. In interphase cells, MTs reorganize into cortical networks tethered to the plasma membrane (PM),

which serve as tracks for PM-localized cellulose synthase complexes (CSCs) and thereby define the direction of cellulose deposition (Paredes *et al.*, 2006; Liu *et al.*, 2015). In addition to their important roles in development, MT arrays function during growth adaptation in response to changing environmental conditions, thereby contributing to plant fitness (Wasteneys and Yang, 2004a).

To engage in these diverse cellular functions, MT organization and dynamics are tightly controlled (Wasteneys, 2002). Developmental and environmental stimuli can induce rapid reorganization of the MT cytoskeleton (e.g. in response to mechanical stimulation) which can occur within a few minutes and involves changes in MT trajectories, as well as altered rates of (de-) polymerization (Hardham *et al.*, 2008). Phytohormones exert control over MT orientation (Shibaoka, 1994; Locascio *et al.*, 2013; Takatani *et al.*, 2015), and signaling via the second messenger calcium (Ca^{2+}) has been implicated in cytoskeletal control, as suggested by sensitivity of MT stability to elevated Ca^{2+} concentrations (Hepler, 2005, 2016). MT-associated proteins (MAPs), which bind to tubulin subunits, play essential roles for regulating cytoskeletal behavior (Lloyd and Hussey, 2001; Sedbrook, 2004) and are likely candidates to integrate incoming signals into appropriate responses. Numerous MAPs have been identified in plants, which mediate bundling, cross-linking, nucleation, or severing of MTs, or, in the case of plus end-tracking MAPs, control dynamic instability at polymerizing plus ends (Akhmanova and Steinmetz, 2008; Horio and Murata, 2014). Other MAPs facilitate physical connections between MTs and protein complexes, such as CSCs (Bringmann *et al.*, 2012), or cross-linking to the actin cytoskeleton (Schneider and Persson, 2015). MAPs also mediate tethering of MTs to the PM (Bayer *et al.*, 2017; Oda, 2018), which is required for stabilization against the pushing forces of CSCs (Liu *et al.*, 2016) and potentially contributes to subcompartmentalization of PMs into functional subdomains (Sugiyama *et al.*, 2017). Still, the modes by which external signals are integrated into MT (re-) orientation and how MAPs contribute to it are poorly understood.

We previously identified IQ67 DOMAIN (IQD) family proteins as the largest known class of MAPs in plants (Bürstenbinder *et al.*, 2017b), which are encoded by multigene families of 23–66 members in several angiosperms, including *Arabidopsis thaliana*, *Oryza sativa* (rice), *Solanum lycopersicum* (tomato), and *Glycine max* (Abel *et al.*, 2005; Huang *et al.*, 2013; Feng *et al.*, 2014). The family-defining IQ67 domain harbors motifs with predicted roles in binding to calmodulin (CaM) Ca^{2+} sensor proteins that are an integral part of the cellular Ca^{2+} decoding machinery (Abel *et al.*, 2005). Thus, IQDs are likely candidates for integration of CaM-dependent Ca^{2+} signaling into MT (re-)organization and growth regulation (Bürstenbinder *et al.*, 2017a). First experimental data point to important roles for IQD proteins in plant development, as indicated by altered fruit shape and grain size in plants with elevated expression levels of tomato *SUN/IQD12* and rice *GRAIN SIZE ON CHROMOSOME 5(GSE5)/IQD21*, respectively (Xiao *et al.*, 2008; Duan *et al.*, 2017). Functions of IQDs in MT organization are supported by differential MT patterns, which are induced upon overexpression of individual

family members in transient expression assays in *Nicotiana benthamiana* (Bürstenbinder *et al.*, 2017b). Divergent MT patterns in *N. benthamiana* correlate with divergent effects on MT organization and growth in transgenic *Arabidopsis IQD* overexpression plants, as indicated by altered plant morphology and cell shape upon ectopic overexpression of, for example, *IQD14* and *IQD16* visible during development and in diverse tissues (Bürstenbinder *et al.*, 2017b). Mechanistic studies on IQD functions, however, are still limited because (i) phenotypes are almost exclusively reported in *IQD* gain-of-function or overexpression lines; (ii) multigene families are not easily amenable to reverse genetics approaches due to functional redundancies; and (iii) insights into the spatial and temporal control of Ca^{2+} signal generation during development are sparse due to limited sensitivities of intracellular Ca^{2+} imaging methods (Kudla *et al.*, 2018).

To identify functions of family members, we selected *Arabidopsis IQD5*, because MT pattern analysis upon overexpression of *YFP-IQD5* in transient expression assays in *N. benthamiana* suggested unique and specific roles for this family member in MT organization (Bürstenbinder *et al.*, 2017b). Moreover, *IQD5*, which belongs to phylogenetic subgroup IIIa of the IQD family, clusters separately from the other members of this subgroup, namely *IQD6–IQD10* (Abel *et al.*, 2005), and thus may have specialized functions *in planta*. In this study, we present a systematic analysis of *Arabidopsis IQD5* using reverse genetics approaches. We identified expression domains of *IQD5* by analysis of transgenic *pIQD5::GFP-GUS* reporter lines, and determined its subcellular localization in transgenic *pIQD5::IQD5-GFP/iqd5-1* lines. We show that *IQD5*–green fluorescent protein (GFP) decorates cortical MTs at neck regions of leaf epidermis pavement cells (PCs). Loss of *IQD5* results in strongly reduced growth restriction at neck regions, which correlates with a reduced deposition of cellulose in anticlinal walls of PCs. Recombinant *IQD5* interacts with apo-CaM and Ca^{2+} -CaM *in vitro*, and *IQD5* recruits CaM to MTs *in planta*. Moreover, we show that PC shape is sensitive to elevated external Ca^{2+} concentrations. Together, our research provides evidence for functions of *IQD5* in shape establishment of leaf epidermis PCs and for the first time links Ca^{2+} signaling to the control of interdigitated growth of PCs.

Materials and methods

Plant material, growth conditions, and macroscopic phenotyping

Wild-type (WT) seeds (Col-0 accession) were originally obtained from the Arabidopsis Biological Resource Center. T-DNA insertion lines SALK_015580 and GK-288E09, referred to as *iqd5-1* and *iqd5-2*, respectively, were obtained from the Nottingham Arabidopsis Stock Centre. Genomic DNA was extracted as described in Bürstenbinder *et al.* (2007). Homozygous mutant lines were identified by PCR-based genotyping with the following primer combinations: *iqd5-1*, WT allele *IQD105* (5'-GATTATCTCTGCCAAACAGCG-3') and *IQD106* (5'-GGAGAGTGACTTGGGCTGAC-3'), insert *IQD105+A004* (5'-ATTTTGCCGATTTTCGGAAC-3'); *iqd5-2*, WT allele *IQD075* (5'-ATGGGAGCTTCAGGGAGATG-3')+*IQD076* (5'-GCGTTACAGCAGCTTGTTTTTC-3'), and insert *IQD076+A009* (5'-ATAATAACGCTGCGGACATCTACATT-3'). A 2201 bp (*pIQD5_{long}*) and a 1207 bp (*pIQD5_{short}*) fragment of the *IQD5* promoter sequence were amplified from genomic DNA with *IQD180*

(5'-CACCTCTATATATGGTTTACAATCGAGACAC-3') and IQD345 (5'-CACCATAAATCACATCACTGTTTTTGGGT-3') forward primers, respectively, in combination with the IQD181 reverse primer (5'-TCTATCTCAATTCACACGATCAG-3'), and mobilized into the pENTR/dTOPO vector. A genomic *pIQD5_{short}::IQD5(w/-stop codon)* fragment was amplified with forward primer IQD1521 (5'-attB1-TCTCTATATATGGTTTACAATCGAGACAC-3') and reverse primer IQD1522 (5'-attB2-CTGCAAGCCTCTGTTTTATTGGGTCGG-3'), and mobilized into pDONR221. Fidelity of inserts was verified by sequencing. For generation of transgenic *pIQD5::GFP-GUS* and *pIQD5::IQD5-GFP* lines, the inserts were mobilized into pBGWFS7 and pB7FWG,0, respectively (Karimi *et al.*, 2002). Arabidopsis plants were transformed by *Agrobacterium tumefaciens*-mediated transfection using the floral dip method (Clough and Bent, 1998). Per construct, 10–24 independent lines were identified in the T₁ generation by Basta selection. T₂ plants were screened for the presence of single-copy T-DNA insertion by segregation analysis (Basta). For analysis of GFP fluorescence and β -glucuronidase (GUS) expression, 2–4 homozygous T₃ lines were included, which showed representative GFP fluorescence or GUS expression patterns.

Seeds were surface sterilized with chlorine gas, stratified for 2 d at 4 °C on *Arabidopsis thaliana* Salts (ATS) medium [1× ATS, 0.5% (w/v) agar gel, 1% (w/v) sucrose] (Lincoln *et al.*, 1990), and grown at 21°C under long-day conditions (16 h light, 8 h dark). For oryzalin treatments, seedlings were incubated for 1–2 h in liquid medium supplemented with 10 μ M oryzalin in a final concentration of 0.25% (v/v) DMSO or the DMSO control as described in Bürstenbinder *et al.* (2013). Macroscopic growth parameters were analyzed in 5-day-old seedling and in 3-week-old plants. Root length was quantified with RootDetection (<http://www.labutils.de/rd.html>, last accessed 19 November 2018). Cotyledon and leaf area were measured with the Easy Leaf Area software (<http://www.plant-image-analysis.org/software/easy-leaf-area>, last accessed 19 November 2018) according to the manual. For treatment with Ca²⁺, seedlings were grown for 5 d on half-strength Murashige and Skoog (1/2 MS) medium supplemented with the indicated concentrations of CaCl₂ according to Chen *et al.* (2014).

RNA extraction and expression analysis

Total RNA was extracted from 2-week-old plants using TRIzol reagent. Synthesis of cDNA via reverse transcription and RT-PCRs were performed according to Bürstenbinder *et al.* (2007) with the following primers: *IQD5*, primer IQD075 and IQD117 (5'-CTATGCAAGCCTCTGTTTTATTGG-3'); *ACTIN2*, primer A005 (5'-CAAAGACCAGCTCTTCCATC-3'); and A006 (5'-CTGTGAACGATTCCTGGACCT-3'). For quantitative real-time PCR (qRT-PCR), conditions were selected as described in Bürstenbinder *et al.* (2017b) and the following primers were used: *IQD5*, IQD1777 (CAACTAAAGCCAACCGAGCA-3') and IQD1778 (GGTTTTGGGCAGATTTTCC-3'), *PP2A* A015 (AGCCAAGTACGACGATCTGGT-3') and A016 (CTATCCGAAGTCTGCCTCATTA-3'). In brief, 3–5 shoots of 2-week-old plants were pooled for RNA extraction. A 2 μ g aliquot of DNase I-treated RNA was reverse transcribed with oligo(dT) primers using the Revert Aid First Strand cDNA synthesis kit (Thermo Fisher) to generate first-strand cDNA. Primer efficiencies were calculated from standard curves. A 1 μ l aliquot of 1:10-diluted cDNA was used in a 10 μ l reaction mix including Fast SYBR Green master mix (Applied Biosystems), and qPCRs were run on a 7500 Fast Real-Time PCR system with the following program: 10 min, 95 °C; 40 cycles of 3 s, 95 °C, and 30 s, 63 °C. Expression levels of *IQD5* were calculated relative to *PP2A*.

Microscopy, staining procedures, and image analysis

Whole-mount GUS staining of seedlings and plants was performed as described in Bürstenbinder *et al.* (2017b). Plant materials were cleared in chloral hydrate, and roots and seeds were imaged with a Zeiss axioplan 2 microscope using a differential interference contrast (DIC) objective. Imaging of whole seedlings, leaves, flowers, and siliques was performed with a Nikon SMZ 1270 stereo microscope.

Confocal imaging was performed with a Zeiss LSM 780 inverted microscope using a $\times 40$ water immersion objective, unless stated otherwise. Generation of yellow fluorescent protein (YFP)–IQD5, Y_N–TRM1, red fluorescent protein (RFP)–TUA5, and mCherry–CaM2 is described in Bürstenbinder *et al.* (2017b) and Gantner *et al.* (2018). GFP was excited using a 488 nm laser and emission was detected between 493 nm and 555 nm. YFP was excited by a 514 nm laser, and emission was detected between 525 nm and 550 nm. For mCherry excitation, a 555 nm laser was used, and emission was detected between 560 nm and 620 nm. Fluorescence intensities of IQD5–GFP adjacent to the periclinal wall at convex and concave sides of lobes were quantified according to Armour *et al.* (2015). Average fluorescence intensities were measured with Fiji (Schindelin *et al.*, 2012) in a total of six cells from three independent seedlings, and five lobes per cell were analyzed. The vector series of Gehl *et al.* (2009) was used for generation of the bimolecular fluorescence complementation (BiFC) construct. For all samples included in the BiFC experiment, imaging was performed with an identical laser setting. In co-expression assays, mCherry and GFP fluorescence were recorded in the sequential mode.

For visualization of cell contours, cell outlines were visualized by propidium iodide (PI) staining as described in Bürstenbinder *et al.* (2017b), and imaged with a $\times 20$ objective [5–10 days after germination (DAG)] or with a $\times 40$ objective (2 and 3 DAG). PI was excited with a 555 nm laser, and emission was detected between 560 nm and 620 nm. Segmentation, feature quantification, and graphical visualization of PC shapes were conducted with the ImageJ plugin PaCeQuant and the associated R script (Möller *et al.*, 2017). For cells in cotyledons 5–10 DAG and in the third true leaf, the threshold for size filtering implemented in PaCeQuant was set to the default value of 240 μ m². For cells in cotyledons 2 and 3 DAG, the threshold for size filtering was reduced to 75 μ m². For time series analysis of cells during cotyledon development, cells were grouped by their sizes into the following categories: tiny <240 μ m²; small, 240–1400 μ m²; medium, 1400–4042 μ m²; and large >4042 μ m². Thresholds for small, medium, and large cells were chosen according to Möller *et al.* (2017).

For histochemical cellulose staining in cell walls, 5-day-old seedlings were incubated for 90 min in 0.04% (v/v) calcofluor white M2R dissolved in Tris–HCl buffer (pH 9.2). To stain callose and the cuticle, seedlings were incubated for 3 h and 5 min in 0.1% (v/v) aniline blue in 100 mM Na₂PO₄ buffer (pH 7.2) and 0.1% (w/v) auramine O in 50 mM Tris–HCl buffer (pH 7.2), respectively. Subsequently, seedlings were co-stained with PI to visualize cell contours. Dissected cotyledons were imaged with a Zeiss LSM 700 inverted microscope, using a $\times 40$ water immersion objective. Calcofluor white, aniline blue, and auramine O were excited with a 405 nm laser, and emission was detected with a 490 nm short pass filter. Co-staining was recorded in the sequential mode.

To quantify fluorescence intensities along the boundaries of the cells, we established a workflow combining automatic segmentation based on the method implemented in PaCeQuant and quantification of fluorescence intensities along the contour segments. For each boundary pixel in an image, the set of adjacent cell regions in a 15 \times 15 neighborhood around the pixel is determined and the fluorescence intensity value of the pixel is added to the total intensity sum of each of these regions. Finally, an average intensity value for the boundary of each cell region is calculated by dividing the intensity sum of the region through the total number of pixels that contributed to the specific region, which we implemented in MiToBo (Möller *et al.*, 2016).

Structure prediction, protein expression, and calmodulin binding assays

Structural prediction of the IQ67 domain of IQD5 spanning amino acids E87–L153 was performed using PHYRE2 (Kelley *et al.*, 2015), which revealed the highest similarities with the crystal structures of the CaM-binding domains of mouse myosin V (PDB:2IX7, 99.5% similarity) (Houdusse *et al.*, 2006) and mouse myosin-1c (PDB:4R8G, 99.8%) (Lu *et al.*, 2015). The predicted structure of the IQ67 domain of IQD5 was aligned with PDB:2IX7, which contains the crystal structure of apo-CaM bound to the first two IQ motifs of myosin V, using PyMol (DeLano, 2009). CaM was fitted to adjust for the different spacing of IQ

motifs by 11 and 12 amino acids in the CaM-binding domains of IQD5 and myosin V, respectively.

Expression of glutathione *S*-transferase (GST)–IQD5 and *in vitro* CaM binding assays were performed according to Levy et al. (2005). Generation of IQD5 pENTR vectors is described in Bürstenbinder et al. (2017b). The coding sequence (CDS) of IQD5 was mobilized into the pDEST15 vector (Invitrogen) to generate an N-terminal GST fusion, and GST–IQD5 and the GST control were expressed in the *Escherichia coli* strain KRX (Novagen) upon induction with 0.1% (w/v) rhamnose and 1 mM isopropyl- β -D-thiogalactopyranoside (IPTG). Cells were resuspended in CaM pull-down buffer [5.8 mM Tris–HCl, pH 7.3; 2.7 mM KCl; 127 mM NaCl; 0.1% (v/v) Tween 20; 0.002% (w/v) NaN₃]. Bovine CaM immobilized on Sepharose beads (GE Healthcare) was incubated with cleared protein extracts in CaM buffer containing either 5 mM EGTA or 1 mM CaCl₂. After four steps of washing, the last washing fraction and the bead fraction were collected, and, together with the unbound fraction, separated by SDS–PAGE. GST-tagged proteins were visualized by immunoblot analysis using a horseradish peroxidase (HRP)–coupled α -GST antibody (Santa Cruz).

Statistical analysis

Statistical analysis of root length, cotyledon and leaf area, and IQD5 expression was performed using ANOVA implemented in the R software, followed by a Tukey's post-hoc test, and Benjamini–Hochberg adjustment of *P*-values. For statistical analysis of fluorescence intensities at convex and concave sides of pavement cells in *pIQD5::IQD5-GFP* seedlings, a *t*-test was performed. Statistical analysis of PC shape features was performed using the Kruskal–Wallis test, followed by a Dunn's post-hoc test and Benjamini–Hochberg adjustment of *P*-values, which is part of the R script provided in the PaCeQuant package.

Results

IQD5 is expressed in vegetative tissues

To identify *in planta* sites of IQD5 function, we determined spatio-temporal expression domains of IQD5 in transgenic *pIQD5_{short}::GFP-GUS* and *pIQD5_{long}::GFP-GUS* reporter lines, in which a 1207 bp and 2201 bp DNA fragment upstream of the translational start site of the IQD5 gene were fused to the reporter, respectively. Histochemical GUS analysis of *pIQD5_{short}::GFP-GUS* lines throughout development revealed strong promoter activity in cotyledons and leaves, in the vasculature of leaves and the hypocotyl, as well as in the shoot apical meristem (Fig. 1A). In roots, GUS staining was detectable mostly in older parts of the root. In root tips, IQD5 promoter activity was restricted to the lateral root cap of primary and lateral root meristems. GUS activity was largely absent from reproductive organs, such as flower buds, flowers, siliques, and seeds, and during embryo development. The GUS patterns are consistent with developmental IQD5 expression data obtained from publicly available microarray data sets (Fig. 1B) (Winter et al., 2007), which confirm higher IQD5 expression levels in vegetative tissues when compared with reproductive tissues. Similar expression patterns were observed in *pIQD5_{long}::GFP-GUS* lines (Supplementary Fig. S1 available at JXB online), suggesting that the 1207 bp fragment was sufficient to report authentic IQD5 expression patterns. Our analysis thus reveals preferential expression of IQD5 in vegetative tissues of shoots and roots.

IQD5–GFP localizes to cortical microtubules

To examine the subcellular localization of IQD5, we generated a fluorescent protein fusion construct, in which GFP was fused to the C-terminus of IQD5 within a genomic fragment containing the native *IQD5_{short}* promoter (Fig. 2). The *pIQD5::IQD5-GFP* construct was introduced into an *iqd5* knockout background to avoid dosage effects of IQD5 copy number (Fig. 2A,B). We obtained two independent Arabidopsis T-DNA insertion lines for IQD5, which we termed *iqd5-1* and *iqd5-2* (Fig. 2A). RT–PCR analysis revealed the complete absence of full-length IQD5 transcripts in *iqd5-1* and *iqd5-2* lines when compared with the WT, demonstrating that both T-DNA insertion lines are null mutant alleles (Fig. 2B). Based on macroscopic examination, both *iqd5* mutants were phenotypically indistinguishable from WT plants, as shown for root length and shoot growth (Supplementary Fig. S2). The *iqd5-1* mutant was transformed with the *pIQD5::IQD5-GFP* construct by *Agrobacterium*-mediated floral dip. qRT-PCR analysis of steady-state IQD5 mRNA levels revealed comparable expression in two independent *pIQD5::IQD5-GFP/iqd5-1* complementation lines, which was moderately higher than in the reference WT (Fig. 2C).

We investigated the subcellular localization of IQD5–GFP by confocal imaging and observed that IQD5 localized in punctate patterns along filamentous structures at the cell cortex of hypocotyl cells, reminiscent of cortical MTs (Fig. 2D). Treatment with oryzalin, a drug that binds to tubulin subunits and prevents MT polymerization (Morejohn et al., 1987), abolished IQD5–GFP localization to filaments, while MTs remained intact upon mock treatment (Fig. 2D). Transgenic *pCaMV 35S::GFP-MAP4* (Marc et al., 1998) and *pCaMV 35S::GFP-ABD2* (Sheahan et al., 2004; Wang et al., 2004) lines were included as controls for the MT and actin cytoskeleton, respectively (Fig. 2D). While oryzalin treatment disrupted MTs decorated with GFP–MAP4, labeled (GFP–ABD2) actin filaments remained intact, demonstrating the efficiency and specificity of the treatment. Co-expression of *pCaMV 35S::YFP-IQD5* with *pCaMV 35S::RFP-TUA5* in transient expression assays in *N. benthamiana* further corroborated colocalization of YFP–IQD5 with MTs (Fig. 2E). GFP fluorescence was very weak in hypocotyls of *pIQD5::IQD5-GFP/iqd5-1* seedlings. Moderately stronger IQD5–GFP fluorescence was detectable at cortical MT arrays in epidermal PCs of cotyledons (Fig. 2F). PCs adopt highly complex jigsaw puzzle-like shapes with interlocking lobes and necks. Within individual PCs, IQD5–GFP accumulated at the convex side of necks at the interface of anticlinal and outer periclinal walls, as indicated by increased average fluorescence intensities when compared with the concave side (Fig. 2F,G).

Loss of IQD5 causes aberrant PC shape

To assess whether IQD5 contributes to growth regulation of PCs, we analyzed PC shapes in cotyledons of *iqd5* mutants and of the two *pIQD5::IQD5-GFP/iqd5-1* lines. Cell outlines were visualized by PI staining, and groups of PCs on the adaxial

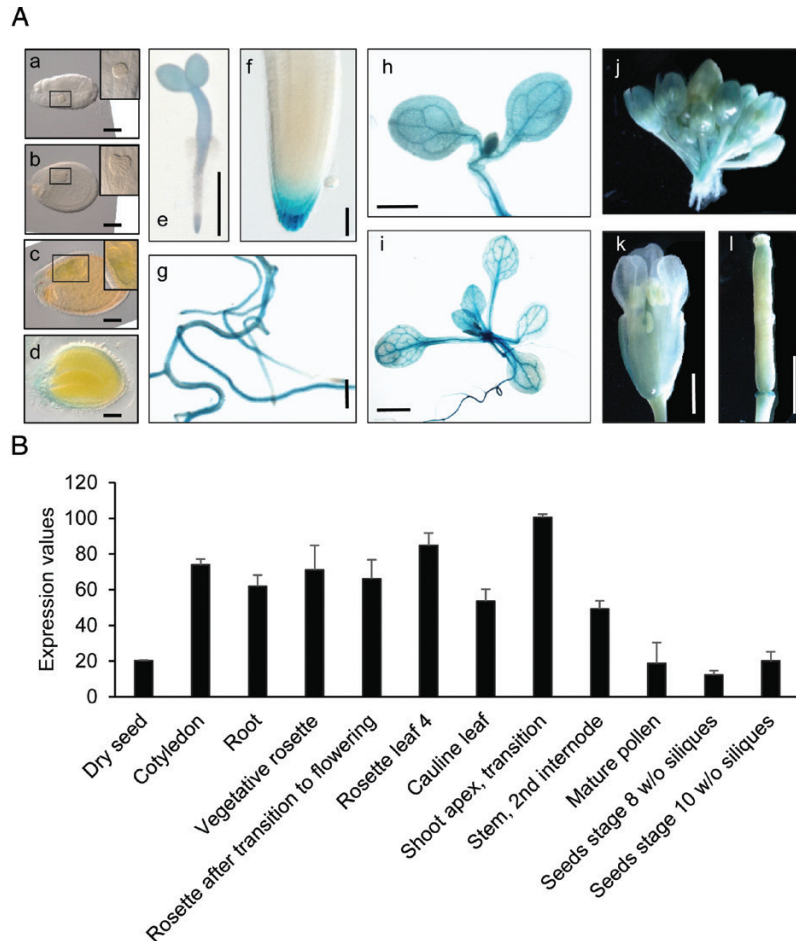


Fig. 1. *IQD5* expression analysis. Whole-mount histochemical GUS staining of *ProIQD5_{short}::GFP-GUS* reporter lines (A) in seeds and embryos of globular (a), heart (b), torpedo (c), and mature (d) stage, in 2-day-old seedlings (e); insets show close-ups of embryos, indicated by black boxes (a–c), in the primary root meristem (f), in lateral roots (g), and in cotyledons (h) of 5-day-old seedlings, in the shoot of 10-day-old seedlings (i), and in flower buds (j), flowers (k), and siliques (l) of 5-week-old plants. Scale bars represent 100 μm (a–d), 1 mm (e, g–l), and 10 μm (f). *In silico* expression data of *IQD5* in different tissues and organs were obtained from the publicly available eFP browser database (<http://bar.utoronto.ca/efp/cgi-bin/efpWeb.cgi>, last accessed 19 November 2018) (B). Data show mean values \pm SD from three independent biological experiments.

side of cotyledons from 5-day-old seedlings were imaged by confocal microscopy (Fig. 3A). PC shape features were quantified with PaCeQuant (Möller *et al.*, 2017), an ImageJ-based open source tool for fully automatic quantification and graphical visualization of PC shape features. As evidenced by similar areas of individual cells and similar area distributions, expansion was largely unaffected in *iqd5* mutants (Fig. 3B). Cell shapes on the other hand differed strongly in both *iqd5* mutant alleles when compared with the WT or the two independent *pIQD5::IQD5-GFP/iqd5-1* lines. Mutants displayed an increased cellular circularity (Fig. 3C). Circularity values range between 0 and 1, where a circularity value of 1 represents a perfect circle. Increased circularity thus indicates reduced cellular complexity in *iqd5* mutants. Reduced cellular complexity correlates with a moderately reduced average number of lobes from 15 lobes per cell in WT to 13 lobes per cell in *iqd5* mutants (Fig. 3D). In addition, *iqd5* mutants displayed a strongly reduced growth of lobes, indicated by an ~30% reduction of average lobe length (Supplementary Fig. S3A). The width of the cellular core region, measured as the maximum (Fig. 3E) core width, was increased by 22%. Maximum core width provides a clearly defined value as an estimate for the

growth restriction of the cellular core region (Möller *et al.*, 2017), which is similar to neck width values manually quantified by, for example, Fu *et al.* (2005). An increased maximum core width indicates reduced growth restriction at neck regions. The phenotypic differences were highly similar between *iqd5-1* and *iqd5-2* mutant alleles. Expression of *pIQD5::IQD5-GFP* in the *iqd5-1* mutant background restored PC shape to WT-like patterns (Fig. 3; Supplementary Fig. S3), which demonstrates functionality of the IQD5–GFP fusion protein and sufficiency of the amplified promoter region for restoring *IQD5* expression levels. Collectively, our data suggest that IQD5 is required for lobe initiation, lobe growth, and growth restriction at neck regions of cotyledon PCs, which is consistent with its predominant localization to cortical MT arrays at necks.

Cell shape defects in iqd5 mutants occur early during cotyledon development

Morphogenesis of PCs in cotyledons is established during distinct phases (Fu *et al.*, 2002; Zhang *et al.*, 2011). In the early phase, 1–3 DAG, lobe formation is initiated and cells start to expand anisotropically, which is followed (3–7 DAG) by diffuse

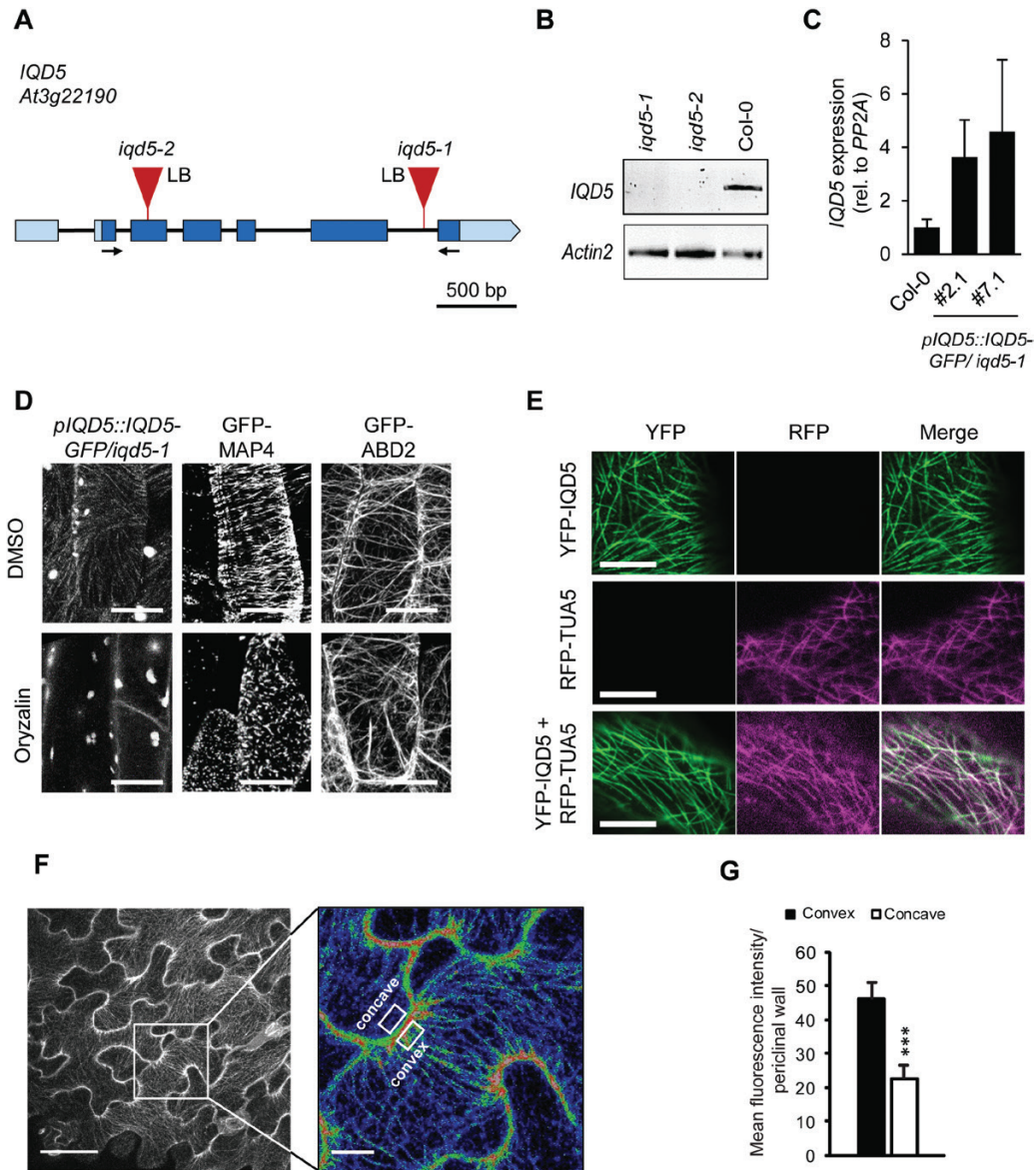


Fig. 2. Subcellular localization of IQD5-GFP in transgenic Arabidopsis *pIQD5::IQD5-GFP/iqd5-1* lines. Gene model and position of T-DNA insertions in two independent mutant lines, *iqd5-1* and *iqd5-2* (A). Boxes indicate the 5'UTR and 3'UTR (light blue), and exons (dark blue). Introns are represented by the black line. Loss of *IQD5* full-length transcript in *iqd5-1* and *iqd5-2* plants compared with the WT (Col-0) was validated by RT-PCR (B). Arrows in (A) indicate the position of primers used for amplification of *IQD5* transcripts. *Actin2* was included as a control for cDNA integrity. Relative *IQD5* expression levels were analyzed by qRT-PCR in two independent transgenic *pIQD5::IQD5-GFP/iqd5-1* lines (#2.1 and #7.1) compared with the WT (C). Data show mean values \pm SD of three independent biological experiments. Subcellular localization of IQD5-GFP in hypocotyls of transgenic *pIQD5::IQD5-GFP/iqd5-1* seedlings after mock (DMSO) or oryzalin (10 μ M) treatment; scale bars=20 μ m (D). Subcellular localization of YFP-IQD5 (top), RFP-TUA5 (middle), and of YFP-IQD5 and RFP-TUA5 (bottom) in transient (co-)expression assays in leaves of *N. benthamiana* (E). Transgenic *pCaMV 35S::GFP-MAP4* and *pCaMV 35S::GFP-ABD2* seedlings were included as controls for the microtubule and actin cytoskeleton, respectively. Z-stack images of GFP fluorescence in epidermis pavement cells of cotyledons from 5-day-old *pIQD5::IQD5-GFP/iqd5-1* seedlings (F). Overview images (left column) and close-up of lobe regions (right column; fluorescence intensities are shown by false coloring, red, high fluorescence intensity; blue, low fluorescence intensity). Scale bars=50 μ m and 5 μ m, respectively. Mean fluorescence intensities measured at the convex and concave side of lobe regions in the upper periclinal wall (G). Data show mean values \pm SD from a total of 50 lobes, quantified in 10 cells from five seedlings.

growth and expansion of shape patterns. Growth ceases at later stages (10–18 DAG), and PCs as well as cotyledons reach their final size (Belteon et al., 2018). To determine at which stage IQD5 functions, we studied PC shape in *iqd5* mutants during cotyledon development and imaged WT and *iqd5* mutant seedlings at 2, 3, 5, 7, and 10 DAG (Fig. 4A). During development, the average cell size increased (Supplementary Figs S4–S8), which is consistent with earlier reports (Zhang et al., 2011;

Möller et al., 2017). To examine shape and geometries in cell populations of similar sizes, referred to as small, medium, and large, we applied the size thresholds of $t_s=1400 \mu\text{m}^2$ and t_m of $4040 \mu\text{m}^2$ at 3, 5, 7, and 10 DAG. These thresholds were experimentally determined in our previous work (Möller et al., 2017), and resemble cells at early (small), intermediate (medium), and late stages of cellular expansion. To distinguish between very small (tiny) and small cell populations in

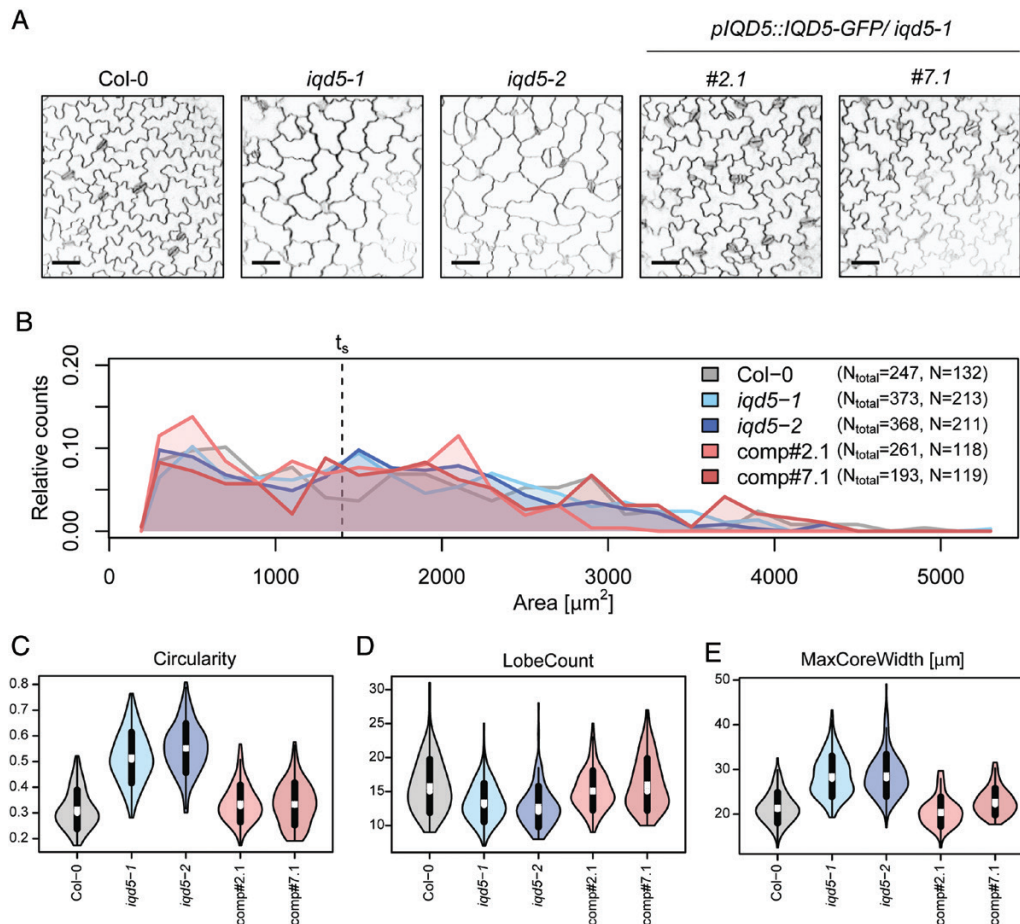


Fig. 3. Pavement cell (PC) morphology on the adaxial side of cotyledons from 5-day-old seedlings of the wild type (Col-0), two independent *iqd5* knockout lines (*iqd5-1* and *iqd5-2*), and two independent transgenic complementation lines (*pIQD5::IQD5-GFP/iqd5-1*; lines #2.1 and #7.1). Representative images of PC morphology (A). Cell outlines were visualized with PI. Images are single optical sections. Scale bars=50 μm . Quantification of cell shape features by PaCeQuant (B–H). Relative distribution of cell areas in the analyzed genotypes (B). Numbers in the key refer to the total number of cells from 10 images of the different genotypes. Cells larger than size threshold $t_s=1400\mu\text{m}^2$ were used for further analysis. Violin plots of feature distributions for circularity (C), lobe count (D), and maximum core width (MaxCoreWidth, E). Circles and crosses refer to medians and means; the vertical black lines represent the SD (thick lines) and the 95% confidence intervals (thin lines). The width of each violin box represents the local distribution of feature values along the y-axis. For an overview of all shape features and statistical analysis, see [Supplementary Fig. S3](#).

cotyledons at 2 and 3 DAG, a time span during which lobe formation and anisotropic expansion are initiated, we included an additional size threshold of $t_{\text{tiny}}=240\mu\text{m}^2$. Quantification of PC shape features revealed first differences in cell shapes of *iqd5* mutants already at 2 and 3 DAG (Fig. 4D, E). When compared with the WT, cellular circularity was moderately but significantly increased in both *iqd5* mutant alleles in tiny and in small-sized cell populations (Fig. 4D), and margin roughness, a measure for the (ir-)regularity of local curvature values along the cell contour, as well as average basal lobe length were reduced (Fig. 4E; [Supplementary Fig. S4](#)). Similar results were observed in seedlings at 3 DAG ([Supplementary Fig. S5](#)). In medium to large-sized cell populations, analyzed in cotyledons between 5 and 10 DAG, phenotypic differences became more pronounced with increasing cell size (Fig. 4F; [Supplementary Figs S6–S8](#)). The time series analysis thus suggests important roles for IQD5 already during early phases of PC morphogenesis in cotyledons. Analysis of *pIQD5_{short}::GFP-GUS* and *pIQD5::IQD5-GFP/iqd5-1* lines revealed promoter activity and accumulation of IQD5-GFP at neck regions, respectively,

in cotyledons and in the shoot apical meristem between 2 and 10 DAG (Fig. 4B, C). Thus, our data demonstrate that *IQD5* is expressed early during cotyledon development and that loss of *IQD5* causes reduced lobe initiation and anisotropic expansion during early growth phases.

IQD5 regulates PC shape during embryogenesis and post-embryonic growth

Cotyledons resemble true leaves in many aspects, and thus provide a convenient system to study leaf development (Tsukaya *et al.*, 1994). However, while cotyledons emerge in embryogenesis, true leaves post-embryonically differentiate from the shoot apical meristem and, unlike cotyledons, differ in their final leaf shape (Tsukaya, 2002). Moreover, some mutations affect exclusively the development of cotyledons or true leaves (Tsukaya, 1995). To test if *IQD5* also functions in true leaf development, we analyzed PC shape in rosette leaves of 3-week-old plants (Fig. 5A). Morphologically, the first two true leaves in Arabidopsis are similar to cotyledons (Poethig, 1997; Kerstetter and Poethig, 1998), and phenotypes in some rosette leaf-specific

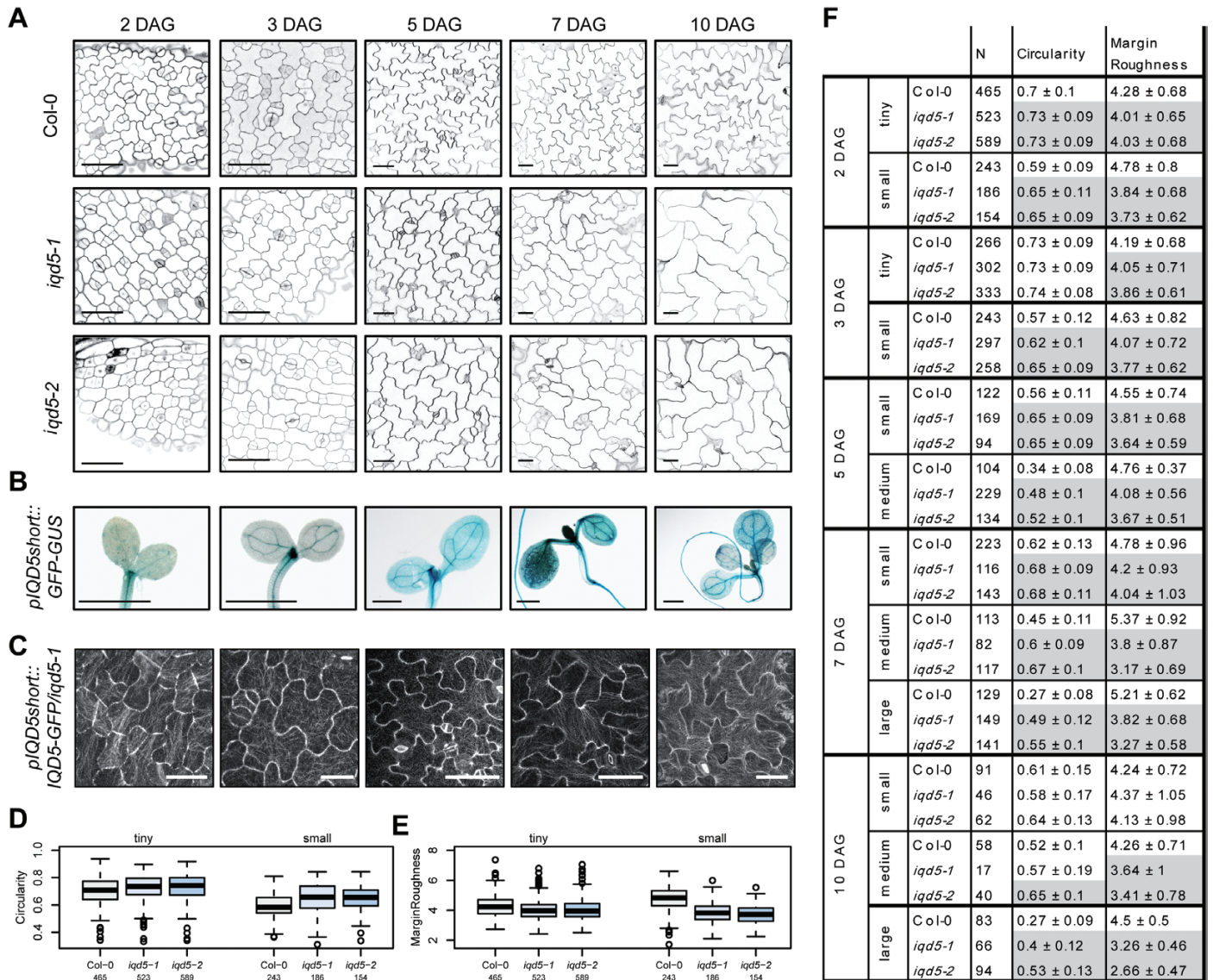


Fig. 4. PC morphology during cotyledon development. Representative images of epidermis cells on the adaxial side of cotyledons of WT, *iqd5-1*, and *iqd5-2* seedlings at 2, 3, 5, 7, and 10 days after germination (DAG) (A). Cell outlines were visualized by PI; scale bars=50 μ m. Histochemical GUS staining of *pIQD5short::GFP-GUS* seedlings at the indicated time points; scale bars=1 mm (B). Analysis of IQD5-GFP subcellular localization in *pIQD5short::IQD5-GFP/iqd5-1* lines at the indicated time points. Scale bars=20 μ m (2 and 3 DAG) and 50 μ m (5–10 DAG) (C). Quantification of PC shape parameters by PaCeQuant. Cell populations were grouped according to their size as tiny, 75–240 μ m², small, 240–1400 μ m², medium 1400–4042 μ m², and large \geq 4042 μ m². Boxplots show feature distributions for circularity (D) and margin roughness (E) in seedlings at 2 DAG. Results are medians; boxes range from the first to third quartile. Feature values for circularity and margin roughness in tiny, small, medium, and large-sized cell populations during cotyledon development (F). Results show mean values \pm SD. Statistically significant differences ($P \leq 0.05$) of *iqd5* mutants relative to the WT are highlighted in gray. For an overview of all shape features and statistical analysis, see [Supplementary Fig. S4–S8](#).

mutants are only visible beyond the second true leaf (Guo et al., 2015). To reflect characteristics of true leaves, we thus focused on the third rosette leaf and analyzed PC shape on the adaxial side (Fig. 5C). Quantification of PC shape features revealed similar shape defects in rosette leaves to those observed for cotyledons. Loss of *IQD5* caused a reduced initiation of lobes, as indicated by reduced lobe counts in *iqd5-1* and *iqd5-2* mutants when compared with the WT (Fig. 5F), and the average lobe length of *iqd5* mutants was reduced (Fig. 5G). Reduced formation and growth of lobes were additionally reflected by increased circularity values (Fig. 5D), as well as reduced margin roughness (Fig. 5E) in PCs of *iqd5* mutant plants. Values of minimum (Supplementary Fig. S9) and maximum core width (Fig. 5H) increased, indicative of reduced growth restriction at

neck regions. *IQD5* thus controls lobe growth and anisotropic expansion in cotyledons and true leaves. In agreement with functions of *IQD5* in true leaves, histochemical GUS activity was detectable in *pIQD5short::GFP-GUS* lines within the entire leaf, indicating that *IQD5* is expressed throughout PC growth (Fig. 5B). Taken together, our data identify *IQD5* as a novel regulator of leaf epidermis PC shape, which controls growth restriction at necks in embryonic and post-embryonic tissues.

Reduced growth restriction correlates with altered cellulose deposition

MTs guide CSCs and determine the deposition and direction of newly forming cellulose fibrils in the cell wall (Paredes

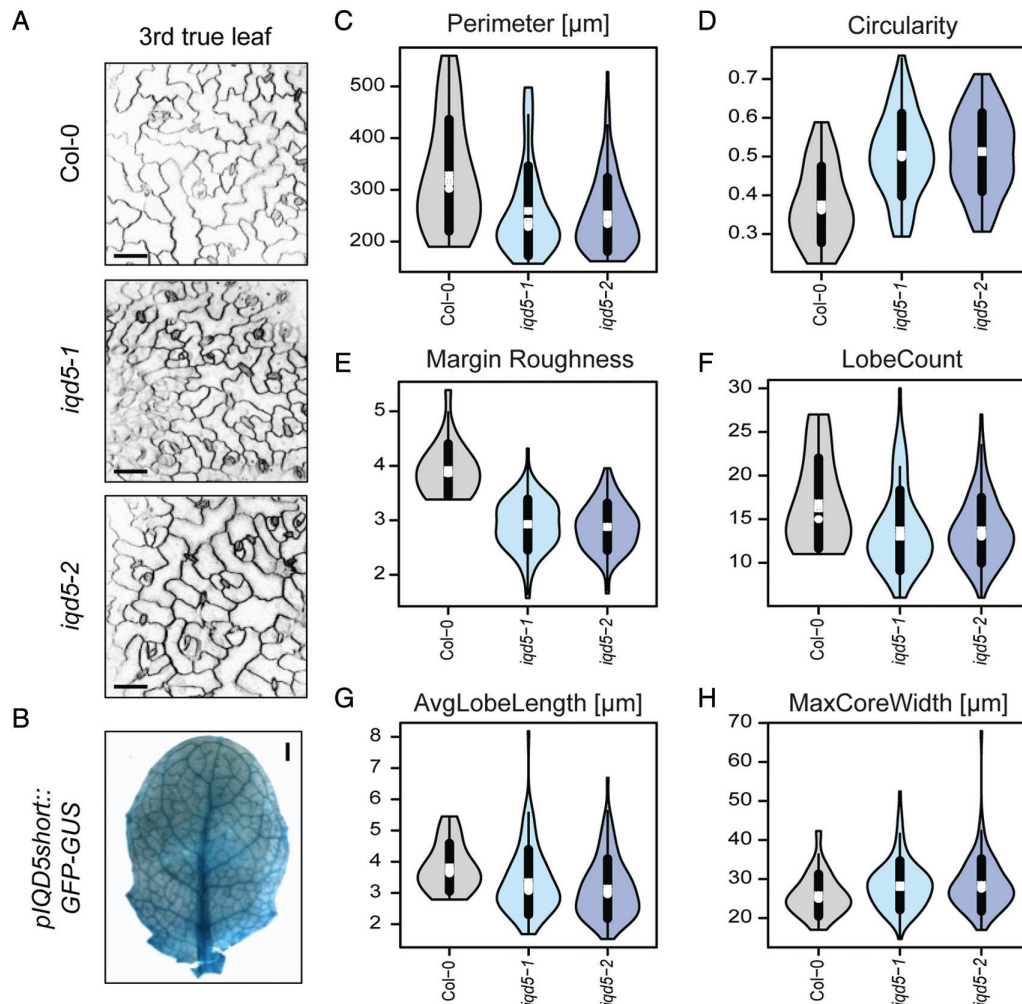


Fig. 5. PC shapes in the epidermis of rosette leaves of the WT and *iqd5* mutants. Images are single optical sections of PI-labeled epidermis cells on the adaxial side of the third rosette leaf in 3-week-old plants; scale bars=50 μm (A). Whole-mount GUS staining of the third rosette leaf in 3-week-old *pIQD5_{short}::GFP-GUS* plants; scale bar=1 mm (B). Quantification of PC shape features. Violin plots show feature distributions from $n=23$ –110 cells from 9–13 images for perimeter (C), circularity (D), margin roughness (E), lobe count (F), average lobe length (G), and maximum core width (H). Circles and crosses refer to medians and means; the vertical black lines represent the SD (thick lines) and the 95% confidence intervals (thin lines). The width of each violin box represents the local distribution of feature values along the y-axis. For an overview of all shape features and statistical analysis, see Supplementary Fig. S9.

et al., 2006; Gutierrez *et al.*, 2009; Endler and Persson, 2011). During cell expansion, cellulose fibrils are aligned perpendicular to the growth axis and promote anisotropic expansion. Because IQD5–GFP labels MTs, and mutants defective in *iqd5* display shape defects reminiscent of decreased growth restriction at necks, we aimed to investigate whether IQD5 affects cellulose deposition. Staining with calcofluor white, a dye used for visualization of cellulose fibrils (Seagull, 1986; Anderson *et al.*, 2010), revealed reduced staining intensities in *iqd5-1* and *iqd5-2* when compared with the WT, which were reverted to WT levels in the complementation line (Fig. 6A). To assess differences in fluorescence intensities at anticlinal cell walls quantitatively, we segmented the contour of individual cells after visualization of cell walls by co-staining with PI using the segmentation mode implemented in PaCeQuant. We measured an $\sim 45\%$ reduction of calcofluor white fluorescence intensities along the cell contour of *iqd5* mutant cells compared with the WT and the complementation line

(Fig. 6D). Reduced intensities suggest reduced deposition of cellulose in anticlinal cell walls of PCs. Calcofluor white, however, does not discriminate between β -1,3- and β -1,4-glucan chains (Anderson *et al.*, 2010), which are the building blocks of callose and cellulose, respectively. To test whether loss of IQD5 specifically affects cellulose deposition, we included aniline blue staining to visualize callose (Wood, 1984) and quantified fluorescence intensities. No differences in callose deposition were observed in the mutants when compared with the WT or the complementation lines (Fig. 6B, E). Similarly, only minor differences (5–10%) in fluorescence intensities were observed upon auramine O staining, which labels the cuticle (Considine and Knox, 1979) (Fig. 6C, F). Taken together, our data suggest that the reduced calcofluor white signals are not an artifact of reduced penetration or uptake of the dyes due to general defects in cell wall composition, and probably reflect reduced cellulose deposition caused by the loss of IQD5.

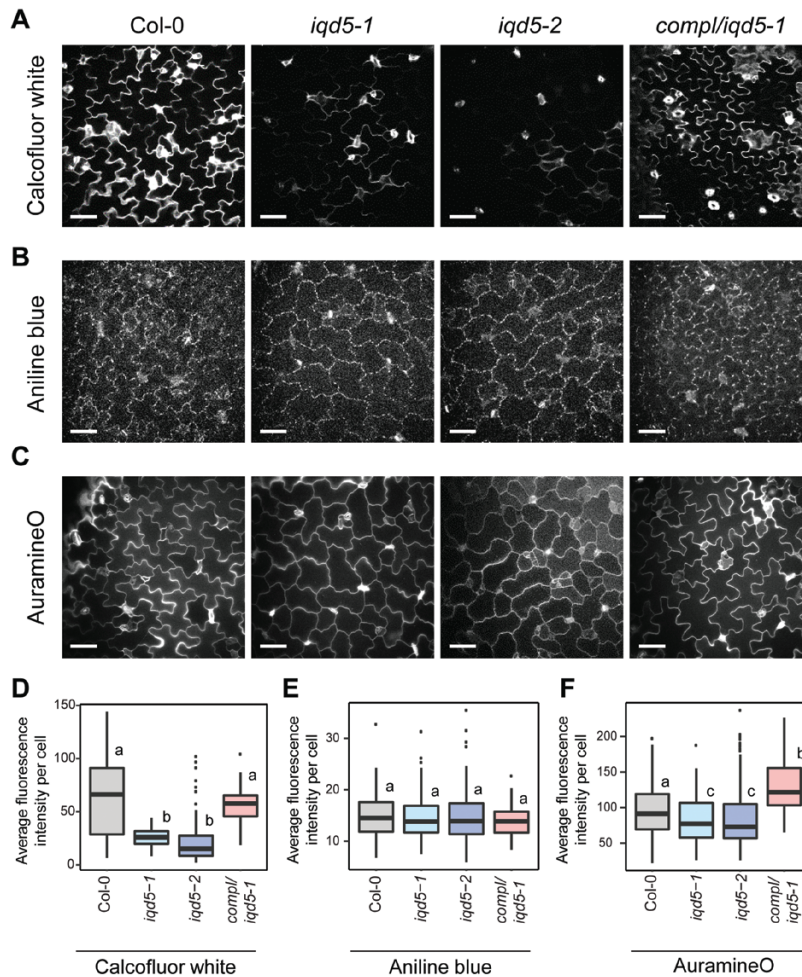


Fig. 6. Histochemical analysis of cell wall composition in the WT, the two *iqd5* mutant alleles *iqd5-1* and *iqd5-2*, and in one transgenic *pIQD5::IQD5-GFP/iqd5-1* line. Confocal images show single optical sections of epidermis pavement cells in cotyledons of 5-day-old seedlings. Cellulose staining by calcofluor white (A), aniline blue staining of callose (B), and auramine O staining of the cuticle (C). Scale bars=50 μ m. Quantification of relative fluorescence intensities along the anticlinal cell wall (D–F). Shown are medians; boxes range from the first to third quartile. Different letters denote a statistically significant difference by one-way ANOVA, $P < 0.01$.

IQD5-dependent recruitment of CaM to cortical microtubules

A hallmark of IQD proteins is the presence of their eponymous IQ67 domain, which contains a repetitive arrangement of predicted CaM-binding motifs (Abel et al., 2005). In IQD5, the IQ67 domain contains three copies each of three different classes of CaM-interacting motifs, including the IQ motif and motifs of the 1-5-10 and 1-8-14 classes, with presumed roles for binding to apo-CaM (IQ) and holo-CaM (1-5-10 and 1-8-14), respectively (Fig. 7A). Homology modeling of IQD5 indicates that the IQ67 domain adopts an α -helical fold (Fig. 7B), similar to the apo-CaM-binding domain of myosin (Houdusse et al., 2006), and potentially interacts simultaneously with more than one CaM polypeptide. To assess whether IQD5 is a functional CaM target, we performed *in vitro* CaM binding assays (Fig. 7C). We expressed GST-tagged IQD5 and the GST core as a control in *E. coli* to investigate interaction with immobilized bovine CaM in the presence (Ca^{2+}) and absence (EGTA) of calcium. GST-IQD5, but not GST, co-sedimented with apo-CaM, and CaM binding of GST-IQD5 was enhanced in the presence of Ca^{2+} . CaM binding thus is

independent of the GST tag, and the predicted CaM-binding motifs (Fig. 7A) are functional in mediating interaction with both states of CaM, the Ca^{2+} -free apo-CaM and Ca^{2+} -bound holo-CaM (Fig. 7C). To gain insight into subcellular sites of IQD5 interaction with CaM, we performed BiFC analyses. N-terminal fusions of IQD5 to the N-terminal half of YFP (Y_N -IQD5) were transiently co-expressed with N-terminal fusions of CaM2 to the C-terminal half of YFP (Y_C -CaM2) in *N. benthamiana* leaves by infiltration with *Agrobacterium* harboring the respective plasmids. As controls, we included Y_N and Y_C fusions of TON1 RECRUITMENT MOTIF1 (TRM1), a member of a plant-specific class of MAPs that interacts with TONNEAU1 (TON1) in *planta* (Drevensek et al., 2012). Recovery of YFP fluorescence was visible along the MT lattice between Y_N -IQD5 and Y_C -CaM2, and between Y_N -TRM1 and Y_C -TON1, which served as positive control (Fig. 7D). No fluorescence complementation was detectable in the negative controls, in which Y_N -IQD5 and Y_C -CaM2 were combined with Y_C -TRM1 and Y_N -TRM1, respectively, demonstrating specificity of the BiFC assay. Additionally, CaM binding at MTs was validated in co-expression assays (Fig. 7E). Expression of *pCaMV 35S::mCherry-CaM2* resulted

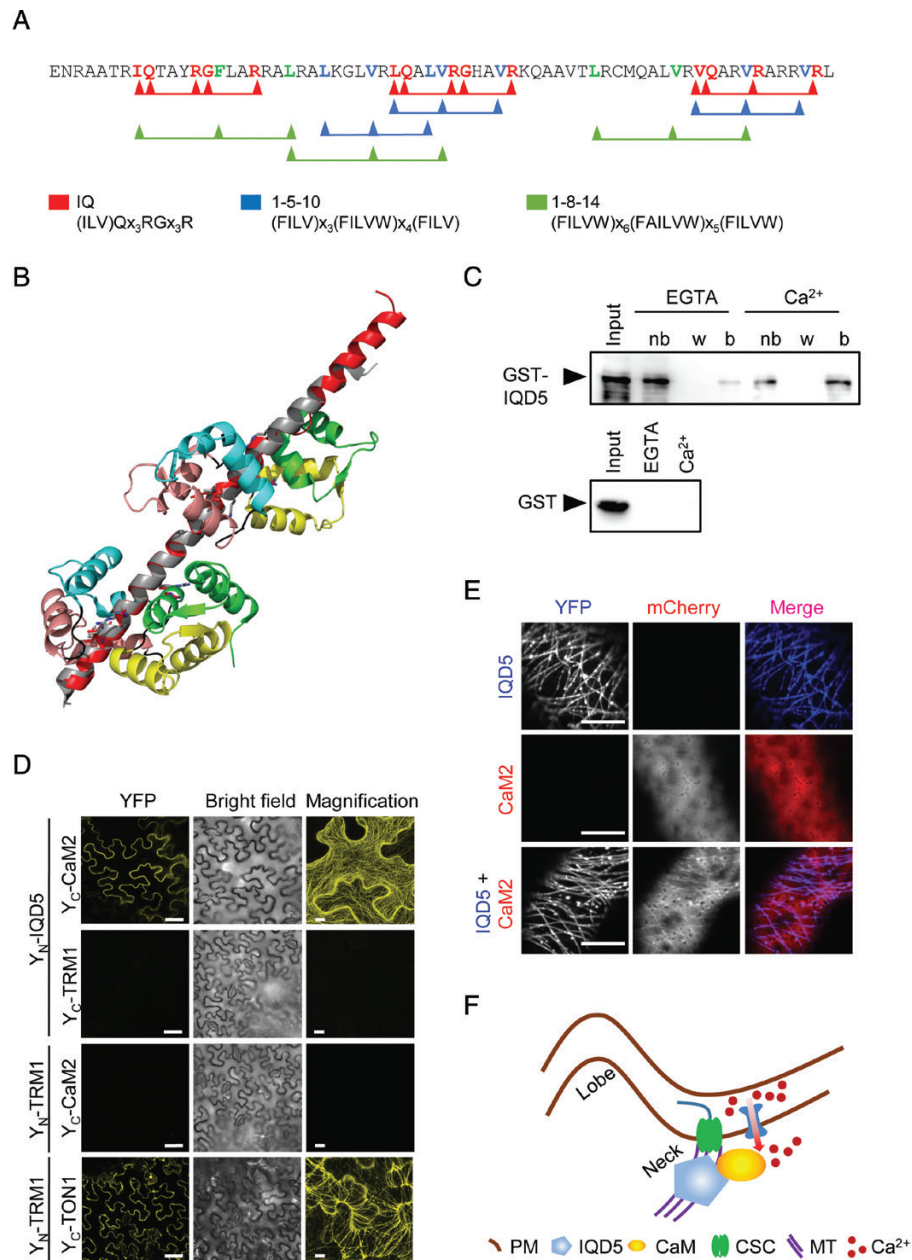


Fig. 7. Calmodulin (CaM) binding properties of IQD5. Amino acid sequence of the IQ67 domain of IQD5 (A). IQ motifs implicated in apoCaM (IQ) and Ca²⁺-CaM (1-5-10 and 1-8-14) binding are highlighted in red, blue, and green, respectively. Structural alignment of the IQ67 domain of IQD5 (red) and the IQ motif-containing domain of myosin (gray), together with two apo-CaM proteins (first, second, third, and fourth EF hand in green, yellow, salmon, and cyan, respectively) (aligned and fitted with PyMol) (B). *In vitro* pull-down of recombinant GST-IQD5 and as control of GST alone expressed in *E. coli* with bovine CaM immobilized on agarose beads in the presence (Ca²⁺) and absence (EGTA) of calcium; nb, not bound; w, last wash; b, bead-immobilized fraction (C). *In planta* interaction of IQD5 with CaM (D, E). BIFC assays between Y_N-IQD5 and Y_C-CaM2 in leaves of *N. benthamiana* (D). Combinations of Y_N-IQD5 with Y_C-TRM1 and Y_C-CaM2 with Y_N-TRM1 served as negative controls. Y_N-TRM1 and Y_C-TON1 were included as positive control. Single optical sections of YFP fluorescence (left column) and corresponding bright field images (center column). Scale bars=50 μm. Right column, close-up Z-stack images of YFP fluorescence; scale bars=10 μm. Subcellular localization of mCherry-CaM2 (top), YFP-IQD5 (middle), and of YFP-IQD5 and mCherry-CaM2 (bottom) in transient (co-)expression assays in leaves of *N. benthamiana* (E). Scale bars=5 μm. Proposed model of IQD5 function in pavement cell morphogenesis (F). IQD5 localizes to microtubules and is required for growth restriction at neck regions, possibly by affecting cellulose deposition along anticlinal cell walls. Interaction of IQD5 with CaM at microtubules points to important roles for Ca²⁺ signaling during shape establishment.

in cytosolic accumulation of mCherry-CaM2, consistent with previous reports (Bürstenbinder *et al.*, 2013). Upon co-expression with YFP-IQD5, mCherry-CaM2 re-localized to cortical MTs (Fig. 7E). Important roles for Ca²⁺ in regulation of PC shape are supported by altered PC morphology in seedlings

grown under elevated concentrations of Ca²⁺ (Supplementary Fig. S10). High external Ca²⁺ resulted in increased circularity and an increased minimum and maximum core width, indicative of a reduced growth restriction at neck regions. Thus, our data point to roles of IQD5 in CaM recruitment to cortical

MTs, and provide the first indications for CaM-dependent Ca^{2+} signaling in shape development of leaf epidermis PCs (Fig. 7F).

Discussion

Plant-specific IQD families emerged as one of the largest class of CaM targets with proposed roles in linking Ca^{2+} signaling to the regulation of plant growth and development (Bürstenbinder *et al.*, 2017b). Despite growing evidence for important roles as cellular scaffolds at the MT cytoskeleton, the precise molecular mechanisms of IQD functions are still enigmatic (Bürstenbinder *et al.*, 2017a). Here, we provide experimental evidence that (i) positions IQD5 at cortical MT arrays in vegetative tissues (Figs 1, 2) and (ii) identifies IQD5 as a novel regulator of shape establishment in epidermal PCs of cotyledons and leaves (Figs 3–5). We further show that (iii) phenotypes in *iqd5* mutants correlate with alteration of cell wall properties (Fig. 6) and (iv) provide experimental evidence for interaction of IQD5 with CaM2 *in vitro* and *in planta* (Fig. 7). Thus, our data support roles for IQD5 in regulation of MTs and cellulose deposition during PC morphogenesis. We further provide the first evidence for roles of Ca^{2+} signaling in the spatial co-ordination of cell expansion during interdigitated growth of PCs.

PCs are the most abundant cell type in the leaf epidermis, which are characterized by their jigsaw puzzle-like shape in Arabidopsis and in several other plant species (Ivakov and Persson, 2013; Jacques *et al.*, 2014). Their morphogenesis relies on lobe initiation and anisotropic expansion to generate the complex multi-lobed shapes of PCs (Zhang *et al.*, 2011). Our study establishes IQD5 as a novel regulator of PC shape formation as revealed by reduced lobe growth and growth restriction of neck regions in PCs of *iqd5* mutants. Lobe initiation, however, is only slightly reduced, and cell size as well as overall growth are unaffected, which indicates that IQD5 specifically functions in control of anisotropic expansion of PCs. Consistent with roles during anisotropic expansion, shape defects in *iqd5* mutants are established during early growth phases (i.e. in cotyledons at 2 DAG) at which lobe formation and lobe growth are initiated, and persist during later growth phases, in which cells expand within the lateral cell borders defined during the early growth phase (Zhang *et al.*, 2011). A role for IQD5 in regulating anisotropic expansion is further supported by its expression pattern identified in *pIQD5::GFP-GUS* reporter lines, which revealed uniform promoter activity within cotyledons and leaves. Similarly, growth and shape changes of PCs occur throughout the entire leaf, and growth rates display large heterogeneity between neighboring cells within expanding leaves (Elsner *et al.*, 2012). In contrast, cell cycle activity ceases in a longitudinal gradient during leaf maturation (Asl *et al.*, 2011). At later growth stages, cell division is restricted to the basal part of cotyledons and leaves, as shown by analysis of the cell division marker *CYCLINB1;1* (*CYCB1;1*) in transgenic *pCYC1;1::GUS* reporter lines (Ferreira *et al.*, 1994; Dhondt *et al.*, 2010; Carter *et al.*, 2017). The combined analysis of mutant phenotypes and of spatio-temporal expression domains

thus establishes IQD5 as a novel factor controlling anisotropic growth of leaf epidermis PCs.

The plant MT cytoskeleton plays important roles in regulation of anisotropic expansion during PC morphogenesis (Fu *et al.*, 2002, 2005; Jacques *et al.*, 2014). Disturbances in MT organization, stability, or dynamics by pharmacological agents or by mutations in MAPs, such as TRM2/LONGIFOLIA1 or KATANIN (KTN1), reduce cellular complexity of PC morphogenesis (Lee *et al.*, 2006; Lin *et al.*, 2013; Akita *et al.*, 2015). Potential roles of IQD proteins as MAPs that control cell expansion are supported by our previous work, which revealed altered MT organization and PC shape in transgenic plants ectopically overexpressing *IQD11*, *IQD14*, or *IQD16* (Bürstenbinder *et al.*, 2017b). Moreover, altered expression of *IQD* genes is linked to regulation of grain size in rice (Duan *et al.*, 2017; Liu *et al.*, 2017; Yang *et al.*, 2018, Preprint) and fruit shape in tomato (Xiao *et al.*, 2008), water melon (*Citrullus lanatus* L.) (Dou *et al.*, 2018), and cucumber (*Cucumis sativus* L.) (Pan *et al.*, 2018), suggesting that IQDs are key determinants of cell and organ shape (Bürstenbinder *et al.*, 2017a). Here, by analysis of GFP fluorescence in transgenic *pIQD5::IQD5-GFP/iqd5-1* lines, we demonstrate subcellular localization of IQD5–GFP to cortical MT arrays in leaf epidermal PCs. Functionality of the GFP-tagged IQD5 protein is indicated by efficient complementation of PC shape defects in *pIQD5::IQD5-GFP/iqd5-1* lines. MT localization was validated by oryzalin treatment in transgenic Arabidopsis plants and by co-localization of YFP–IQD5 with the MT marker RFP–TUA5 in transient expression assays in *N. benthamiana*. Our work thus for the first time identifies a direct link between MTs and cell expansion in an *iqd* knockout mutant. Notably, in contrast to most reported mutants with defects in PC shape that have pleiotropic effects, including reduced plant growth, organ twisting, or swelling of cells (Qian *et al.*, 2009), *iqd5* mutants are macroscopically indistinguishable from the WT. Specific defects in PC morphogenesis thus indicate limited functional redundancy and compensation between the 33 IQD family members in Arabidopsis and point to unique roles for IQD5 in PC morphogenesis.

Quantification of fluorescence intensities along the outer periclinal cell wall suggests accumulation of IQD5–GFP at convex sides of indenting neck regions. Our findings are consistent with *iqd5* mutant phenotypes and patterns of subcellular IQD5 localization reported in an independent study, which was published while our work was under revision (Liang *et al.*, 2018). Similar to IQD5–GFP, preferential accumulation of MT bundles at neck regions has been reported in several studies, and MT accumulation correlates with reduced growth in the neck regions (Fu *et al.*, 2005; Sampathkumar *et al.*, 2014; Armour *et al.*, 2015). Cortical MTs serve as tracks for PM-localized CSCs and thereby determine the direction of cellulose deposition and consequently cell expansion (Endler and Persson, 2011). Here, using histochemical staining, we show that *iqd5* mutants accumulate reduced amounts of cellulose in their anticlinal walls while callose deposition and cuticle formation are unaffected. Plants with impaired cellulose deposition, for example upon cellulase treatment or in mutants of the

cellulose synthase AtCesA1, display strongly reduced lobing of PCs (Higaki *et al.*, 2016; Majda *et al.*, 2017), similar to phenotypes in *iqd5* lines. Our data suggest that IQD5 is required for efficient cellulose deposition, for example by controlling MT dynamics or organization, thereby affecting cellulose synthesis. In agreement with this hypothesis, Liang *et al.* (2018) reported increased disorder of cortical MTs in *iqd5* mutants when compared with the WT and provide first evidence for functions of IQD5 in stabilization of MTs. Alternatively, IQD5 may mediate coupling of cellulose synthase movement to MT tracks, possibly by direct interaction with KINESIN LIGHT CHAIN-RELATED (KLCR)/CELLULOSE MICROTUBULE UNCOUPLING (CMU) family members. KLCRs mediate PM tethering of MTs to stabilize cortical MTs against the pushing forces of CSCs (Liu *et al.*, 2016). Arabidopsis IQD1, IQD2, and IQD23 interact with KLCR family members in yeast, and IQD1 recruits KLCR1 to MTs in transient expression assays in *N. benthamiana* (Mukhtar *et al.*, 2011; Bürstenbinder *et al.*, 2013). Thus, the prospect arises that IQD:KLCR modules collectively co-ordinate MT organization and lateral stability of cortical MTs at the PM–MT nexus.

A hallmark of IQD families is their ability to bind CaM Ca²⁺ sensors, which suggests important roles for IQDs in linking CaM-mediated Ca²⁺ signaling to the regulation of the MT cytoskeleton via as yet unknown mechanisms (Abel *et al.*, 2005, Hepler, 2016; Bürstenbinder *et al.*, 2017b). The phenotypes in *iqd5* mutants, together with the IQD5-dependent recruitment of CaM to cortical MTs, provide the first experimental evidence for functions of Ca²⁺ signaling in PC morphogenesis, probably via CaM/CMLs. Roles for Ca²⁺ during PC morphogenesis are further supported by altered PC shapes in response to elevated exogenous Ca²⁺ supply. Interestingly, IQD5 interacts *in vitro* with both states of CaM, the Ca²⁺-free and Ca²⁺-bound apo- and holoCaM, respectively. Similarly, IQD1 and IQD20 interact with apoCaM and holoCaM *in vitro* (Abel *et al.*, 2005; Bürstenbinder *et al.*, 2013), which suggests functionality of the distinct CaM-binding motifs within the IQ67 domain. The repetitive alignment of multiple CaM-binding motifs may facilitate interaction with several CaM/CMLs simultaneously, in which individual CaM-binding motifs differentially contribute to CaM/CML binding. Additionally, CaM/CMLs may exert specific effects on IQD5 depending on their Ca²⁺ occupancy, which adds another potential layer of Ca²⁺-dependent regulation. Identification of *in planta* IQD5-interacting CaM/CMLs, however, will be challenging because large multigene families of 7 and 50 members code for CaMs and CMLs in Arabidopsis, respectively, and many *CaM/CML* genes are expressed in cotyledons and leaves (Supplementary Fig. S11). Ca²⁺ signals are rapidly generated by exogenous application of several phytohormones, including auxin and cytokinin (Saunders and Hepler, 1981; Vanneste and Friml, 2013), which are key regulators of PC morphogenesis that antagonistically activate Rho-like GTPases from plants (ROPs) in lobes and necks, respectively (Fu *et al.*, 2002, 2005, 2009). IQD5 and related proteins of the IQD family may constitute promising candidates for integrating upstream signals (e.g. from phytohormones) into the reorganization of MT arrays, possibly via phytohormone-induced Ca²⁺ signals (Bürstenbinder

et al., 2017a; this study). Lastly, a recent study by Sugiyama *et al.* (2017) provides first indications for functions of IQD13 in spatial control of ROP signaling domains required for cell wall patterning during vessel development. A similar mechanism might apply to IQD5 during PC shape formation, thereby providing a potential link between phytohormone actions, Ca²⁺ signaling, and ROP GTPase activation. Collectively, our work identifies IQD5 as a novel regulator of PC shape and a potential hub for co-ordination of cellular signaling, cytoskeletal reorganization, and cell wall remodeling. Our work thus provides a framework for future mechanistic studies of cellular signaling networks at the cell wall–PM–MT continuum, which will aid a more holistic understanding of cellular processes guiding shape complexity.

Supplementary data

Supplementary data are available at *JXB* online.

Fig. S1. *IQD5* expression analysis in *pIQD5_{long}::GFP-GUS* reporter lines.

Fig. S2. Macroscopic analysis of growth parameters in the WT and *iqd5* mutants.

Fig. S3. Quantification and statistical analysis of PC shape features in 5-day-old seedlings of the WT and *iqd5* mutants.

Fig. S4. Quantification and statistical analysis of PC shape in cotyledons at 2 DAG.

Fig. S5. Quantification and statistical analysis of PC shape in cotyledons at 3 DAG.

Fig. S6. Quantification and statistical analysis of PC shape in cotyledons at 5 DAG.

Fig. S7. Quantification and statistical analysis of PC shape in cotyledons at 7 DAG.

Fig. S8. Quantification and statistical analysis of PC shape in cotyledons at 10 DAG.

Fig. S9. Quantification and statistical analysis of PC shape in true leaves.

Fig. S10. Calcium-dependent changes in PC shape.

Fig. S11. *In silico* expression analysis of Arabidopsis CaM/CMLs.

Acknowledgements

Funding was provided by the Deutsche Forschungsgemeinschaft (DFG; SFB648 to KB and SA), the German Academic Exchange Service (to DM), the Erasmus Mundus program (to PK), and by core funding of the Leibniz Association. This paper is a joint effort of the working group BIU, a unit of the German Centre for Integrative Biodiversity Research (iDiv) Halle-Jena-Leipzig, funded by the DFG (FZT 118).

References

- Abel S, Savchenko T, Levy M. 2005. Genome-wide comparative analysis of the IQD gene families in *Arabidopsis thaliana* and *Oryza sativa*. *BMC Evolutionary Biology* **5**, 72.
- Akhmanova A, Hammer JA 3rd. 2010. Linking molecular motors to membrane cargo. *Current Opinion in Cell Biology* **22**, 479–487.
- Akhmanova A, Steinmetz MO. 2008. Tracking the ends: a dynamic protein network controls the fate of microtubule tips. *Nature Reviews. Molecular Cell Biology* **9**, 309–322.

- Akita K, Higaki T, Kutsuna N, Hasezawa S.** 2015. Quantitative analysis of microtubule orientation in interdigitated leaf pavement cells. *Plant Signaling & Behavior* **10**, e1024396.
- Anderson CT, Carroll A, Akhmetova L, Somerville C.** 2010. Real-time imaging of cellulose reorientation during cell wall expansion in Arabidopsis roots. *Plant Physiology* **152**, 787–796.
- Armour WJ, Barton DA, Law AM, Overall RL.** 2015. Differential growth in periclinal and anticlinal walls during lobe formation in Arabidopsis cotyledon pavement cells. *The Plant Cell* **27**, 2484–2500.
- Asl LK, Dhondt S, Boudolf V, Beemster GT, Beeckman T, Inzé D, Govaerts W, De Veylder L.** 2011. Model-based analysis of Arabidopsis leaf epidermal cells reveals distinct division and expansion patterns for pavement and guard cells. *Plant Physiology* **156**, 2172–2183.
- Bayer EM, Sparkes I, Vanneste S, Rosado A.** 2017. From shaping organelles to signalling platforms: the emerging functions of plant ER–PM contact sites. *Current Opinion in Plant Biology* **40**, 89–96.
- Belton SA, Sawchuk MG, Donohoe BS, Scarpella E, Szymanski DB.** 2018. Reassessing the roles of PIN proteins and anticlinal microtubules during pavement cell morphogenesis. *Plant Physiology* **176**, 432–449.
- Bringmann M, Li E, Sampathkumar A, Kocabek T, Hauser MT, Persson S.** 2012. POM-POM2/cellulose synthase interacting1 is essential for the functional association of cellulose synthase and microtubules in Arabidopsis. *The Plant Cell* **24**, 163–177.
- Bürstenbinder K, Mitra D, Quegwer J.** 2017a. Functions of IQD proteins as hubs in cellular calcium and auxin signaling: a toolbox for shape formation and tissue-specification in plants? *Plant Signaling & Behavior* **12**, e1331198.
- Bürstenbinder K, Möller B, Plötner R, Stamm G, Hause G, Mitra D, Abel S.** 2017b. The IQD family of calmodulin-binding proteins links calcium signaling to microtubules, membrane subdomains, and the nucleus. *Plant Physiology* **173**, 1692–1708.
- Bürstenbinder K, Rzewuski G, Wirtz M, Hell R, Sauter M.** 2007. The role of methionine recycling for ethylene synthesis in Arabidopsis. *The Plant Journal* **49**, 238–249.
- Bürstenbinder K, Savchenko T, Müller J, Adamson AW, Stamm G, Kwong R, Zipp BJ, Dinesh DC, Abel S.** 2013. Arabidopsis calmodulin-binding protein IQ67-domain 1 localizes to microtubules and interacts with kinesin light chain-related protein-1. *Journal of Biological Chemistry* **288**, 1871–1882.
- Carter R, Sánchez-Corrales YE, Hartley M, Grieneisen VA, Marée AFM.** 2017. Pavement cells and the topology puzzle. *Development* **144**, 4386–4397.
- Chen X, Grandont L, Li H, Hauschild R, Paque S, Abuzeineh A, Rakusová H, Benkova E, Perrot-Rechenmann C, Friml J.** 2014. Inhibition of cell expansion by rapid ABP1-mediated auxin effect on microtubules. *Nature* **516**, 90–93.
- Clough SJ, Bent AF.** 1998. Floral dip: a simplified method for *Agrobacterium*-mediated transformation of *Arabidopsis thaliana*. *The Plant Journal* **16**, 735–743.
- Considine JA, Knox RB.** 1979. Development and histochemistry of the cells, cell walls, and cuticle of the dermal system of fruit of the grape, *Vitis vinifera* L. *Protoplasma* **99**, 347–365.
- DeLano WL.** 2009. PyMOL molecular viewer: updates and refinements. *Abstracts of Papers of the American Chemical Society* **238**.
- Dhondt S, Coppens F, De Winter F, Swarup K, Merks RM, Inzé D, Bennett MJ, Beemster GT.** 2010. SHORT-ROOT and SCARECROW regulate leaf growth in Arabidopsis by stimulating S-phase progression of the cell cycle. *Plant Physiology* **154**, 1183–1195.
- Dou J, Zhao S, Lu X, He N, Zhang L, Ali A, Kuang H, Liu W.** 2018. Genetic mapping reveals a candidate gene (CIFS1) for fruit shape in watermelon (*Citrullus lanatus* L.). *Theoretical and Applied Genetics* **131**, 947–958.
- Drevensek S, Goussot M, Duroc Y, et al.** 2012. The Arabidopsis TRM1–TON1 interaction reveals a recruitment network common to plant cortical microtubule arrays and eukaryotic centrosomes. *The Plant Cell* **24**, 178–191.
- Duan P, Xu J, Zeng D, et al.** 2017. Natural variation in the promoter of *GSE5* contributes to grain size diversity in rice. *Molecular Plant* **10**, 685–694.
- Elsner J, Michalski M, Kwiatkowska D.** 2012. Spatiotemporal variation of leaf epidermal cell growth: a quantitative analysis of *Arabidopsis thaliana* wild-type and triple cyclinD3 mutant plants. *Annals of Botany* **109**, 897–910.
- Endler A, Persson S.** 2011. Cellulose synthases and synthesis in Arabidopsis. *Molecular Plant* **4**, 199–211.
- Feng L, Chen Z, Ma H, Chen X, Li Y, Wang Y, Xiang Y.** 2014. The *IQD* gene family in soybean: structure, phylogeny, evolution and expression. *PLoS One* **9**, e110896.
- Ferreira PC, Hemerly AS, Engler JD, van Montagu M, Engler G, Inzé D.** 1994. Developmental expression of the arabidopsis cyclin gene *cyc1At*. *The Plant Cell* **6**, 1763–1774.
- Fu Y, Gu Y, Zheng Z, Wasteneys G, Yang Z.** 2005. Arabidopsis interdigitating cell growth requires two antagonistic pathways with opposing action on cell morphogenesis. *Cell* **120**, 687–700.
- Fu Y, Li H, Yang Z.** 2002. The ROP2 GTPase controls the formation of cortical fine F-actin and the early phase of directional cell expansion during Arabidopsis organogenesis. *The Plant Cell* **14**, 777–794.
- Fu Y, Xu T, Zhu L, Wen M, Yang Z.** 2009. A ROP GTPase signaling pathway controls cortical microtubule ordering and cell expansion in Arabidopsis. *Current Biology* **19**, 1827–1832.
- Gantner J, Ordon J, Ilse T, Kretschmer C, Gruetzner R, Löffke C, Dagdas Y, Bürstenbinder K, Marillonnet S, Stüttmann J.** 2018. Peripheral infrastructure vectors and an extended set of plant parts for the Modular Cloning system. *PLoS One* **13**, e0197185.
- Gehl C, Waadt R, Kudla J, Mendel RR, Hänsch R.** 2009. New GATEWAY vectors for high throughput analyses of protein–protein interactions by bimolecular fluorescence complementation. *Molecular Plant* **2**, 1051–1058.
- Guo X, Qin Q, Yan J, Niu Y, Huang B, Guan L, Li Y, Ren D, Li J, Hou S.** 2015. TYPE-ONE PROTEIN PHOSPHATASE4 regulates pavement cell interdigitation by modulating PIN-FORMED1 polarity and trafficking in Arabidopsis. *Plant Physiology* **167**, 1058–1075.
- Gutierrez R, Lindeboom JJ, Paredes AR, Emons AM, Ehrhardt DW.** 2009. Arabidopsis cortical microtubules position cellulose synthase delivery to the plasma membrane and interact with cellulose synthase trafficking compartments. *Nature Cell Biology* **11**, 797–806.
- Hardham AR, Takemoto D, White RG.** 2008. Rapid and dynamic subcellular reorganization following mechanical stimulation of Arabidopsis epidermal cells mimics responses to fungal and oomycete attack. *BMC Plant Biology* **8**, 63.
- Hepler PK.** 2005. Calcium: a central regulator of plant growth and development. *The Plant Cell* **17**, 2142–2155.
- Hepler PK.** 2016. The cytoskeleton and its regulation by calcium and protons. *Plant Physiology* **170**, 3–22.
- Higaki T, Kutsuna N, Akita K, Takigawa-Imamura H, Yoshimura K, Miura T.** 2016. A theoretical model of jigsaw-puzzle pattern formation by plant leaf epidermal cells. *PLoS Computational Biology* **12**, e1004833.
- Horio T, Murata T.** 2014. The role of dynamic instability in microtubule organization. *Frontiers in Plant Science* **5**, 511.
- Houdusse A, Gaucher JF, Krementsova E, Mui S, Trybus KM, Cohen C.** 2006. Crystal structure of apo-calmodulin bound to the first two IQ motifs of myosin V reveals essential recognition features. *Proceedings of the National Academy of Sciences, USA* **103**, 19326–19331.
- Huang Z, Van Houten J, Gonzalez G, Xiao H, van der Knaap E.** 2013. Genome-wide identification, phylogeny and expression analysis of *SUN*, *OFP* and *YABBY* gene family in tomato. *Molecular Genetics and Genomics* **288**, 111–129.
- Hussey PJ, Ketelaar T, Deeks MJ.** 2006. Control of the actin cytoskeleton in plant cell growth. *Annual Review of Plant Biology* **57**, 109–125.
- Ivakov A, Persson S.** 2013. Plant cell shape: modulators and measurements. *Frontiers in Plant Science* **4**, 439.
- Jacques E, Verbelen JP, Vissenberg K.** 2014. Review on shape formation in epidermal pavement cells of the Arabidopsis leaf. *Functional Plant Biology* **41**, 914–921.
- Karimi M, Inzé D, Depicker A.** 2002. GATEWAY vectors for *Agrobacterium*-mediated plant transformation. *Trends in Plant Science* **7**, 193–195.
- Kelley LA, Mezulis S, Yates CM, Wass MN, Sternberg MJ.** 2015. The Phyre2 web portal for protein modeling, prediction and analysis. *Nature Protocols* **10**, 845–858.
- Kerstetter RA, Poethig RS.** 1998. The specification of leaf identity during shoot development. *Annual Review of Cell and Developmental Biology* **14**, 373–398.

- Kudla J, Becker D, Grill E, Hedrich R, Hippler M, Kummer U, Parniske M, Romeis T, Schumacher K.** 2018. Advances and current challenges in calcium signaling. *New Phytologist* **218**, 414–431.
- Lee YK, Kim GT, Kim IJ, Park J, Kwak SS, Choi G, Chung WI.** 2006. *LONGIFOLIA1* and *LONGIFOLIA2*, two homologous genes, regulate longitudinal cell elongation in *Arabidopsis*. *Development* **133**, 4305–4314.
- Levy M, Wang Q, Kaspi R, Parrella MP, Abel S.** 2005. Arabidopsis IQD1, a novel calmodulin-binding nuclear protein, stimulates glucosinolate accumulation and plant defense. *The Plant Journal* **43**, 79–96.
- Liang H, Zhang Y, Martinez P, Rasmussen CG, Xu T, Yang Z.** 2018. The microtubule-associated protein IQ67 DOMAIN5 modulates microtubule dynamics and pavement cell shape. *Plant Physiology* **177**, 1555–1568.
- Lin D, Cao L, Zhou Z, Zhu L, Ehrhardt D, Yang Z, Fu Y.** 2013. Rho GTPase signaling activates microtubule severing to promote microtubule ordering in *Arabidopsis*. *Current Biology* **23**, 290–297.
- Lincoln C, Britton JH, Estelle M.** 1990. Growth and development of the *axr1* mutants of *Arabidopsis*. *The Plant Cell* **2**, 1071–1080.
- Liu J, Chen J, Zheng X, et al.** 2017. GW5 acts in the brassinosteroid signalling pathway to regulate grain width and weight in rice. *Nature Plants* **3**, 17043.
- Liu Z, Persson S, Zhang Y.** 2015. The connection of cytoskeletal network with plasma membrane and the cell wall. *Journal of Integrative Plant Biology* **57**, 330–340.
- Liu Z, Schneider R, Kesten C, Zhang Y, Somssich M, Zhang Y, Fernie AR, Persson S.** 2016. Cellulose–microtubule uncoupling proteins prevent lateral displacement of microtubules during cellulose synthesis in *Arabidopsis*. *Developmental Cell* **38**, 305–315.
- Lloyd C, Hussey P.** 2001. Microtubule-associated proteins in plants—why we need a MAP. *Nature Reviews. Molecular Cell Biology* **2**, 40–47.
- Locascio A, Blázquez MA, Alabadi D.** 2013. Dynamic regulation of cortical microtubule organization through prefoldin–DELLA interaction. *Current Biology* **23**, 804–809.
- Lu Q, Li J, Ye F, Zhang M.** 2015. Structure of myosin-1c tail bound to calmodulin provides insights into calcium-mediated conformational coupling. *Nature Structural & Molecular Biology* **22**, 81–88.
- Majda M, Gronos P, Sintorn IM, et al.** 2017. Mechanochemical polarization of contiguous cell walls shapes plant pavement cells. *Developmental Cell* **43**, 290–304.e4.
- Marc J, Granger CL, Brincat J, Fisher DD, Kao Th, McCubbin AG, Cyr RJ.** 1998. A GFP–MAP4 reporter gene for visualizing cortical microtubule rearrangements in living epidermal cells. *The Plant Cell* **10**, 1927–1940.
- Möller B, Glaß M, Misiak D, Posch S.** 2016. MiToBo—a toolbox for image processing and analysis. *Journal of Open Research Software* **4**, e17.
- Möller B, Poeschl Y, Plötner R, Bürstenbinder K.** 2017. PaCeQuant: a tool for high-throughput quantification of pavement cell shape characteristics. *Plant Physiology* **175**, 998–1017.
- Morejohn LC, Bureau TE, Molè-Bajer J, Bajer AS, Fosket DE.** 1987. Oryzalin, a dinitroaniline herbicide, binds to plant tubulin and inhibits microtubule polymerization in vitro. *Planta* **172**, 252–264.
- Mukhtar MS, Carvunis AR, Dreze M, et al.** 2011. Independently evolved virulence effectors converge onto hubs in a plant immune system network. *Science* **333**, 596–601.
- Oda Y.** 2018. Emerging roles of cortical microtubule–membrane interactions. *Journal of Plant Research* **131**, 5–14.
- Pan YP, Liang XJ, Gao ML, Liu HQ, Meng HW, Weng YQ, Cheng ZH.** 2018. Round fruit shape in W17239 cucumber is controlled by two interacting quantitative trait loci with one putatively encoding a tomato SUN homolog. *Theoretical and Applied Genetics* **130**, 573–586.
- Paredez AR, Somerville CR, Ehrhardt DW.** 2006. Visualization of cellulose synthase demonstrates functional association with microtubules. *Science* **312**, 1491–1495.
- Poethig RS.** 1997. Leaf morphogenesis in flowering plants. *The Plant Cell* **9**, 1077–1087.
- Qian P, Hou S, Guo G.** 2009. Molecular mechanisms controlling pavement cell shape in *Arabidopsis* leaves. *Plant Cell Reports* **28**, 1147–1157.
- Sampathkumar A, Krupinski P, Wightman R, Milani P, Berquand A, Boudaoud A, Hamant O, Jönsson H, Meyerowitz EM.** 2014. Subcellular and supracellular mechanical stress prescribes cytoskeleton behavior in *Arabidopsis* cotyledon pavement cells. *eLife* **3**, e01967.
- Saunders MJ, Hepler PK.** 1981. Localization of membrane-associated calcium following cytokinin treatment in *Funaria* using chlorotetracycline. *Planta* **152**, 272–281.
- Schindelin J, Arganda-Carreras I, Frise E, et al.** 2012. Fiji: an open-source platform for biological-image analysis. *Nature Methods* **9**, 676–682.
- Schneider R, Persson S.** 2015. Connecting two arrays: the emerging role of actin–microtubule cross-linking motor proteins. *Frontiers in Plant Science* **6**, 415.
- Seagull RW.** 1986. Changes in microtubule organization and wall microfibril orientation during in vitro cotton fiber development—an immunofluorescent study. *Canadian Journal of Botany* **64**, 1373–1381.
- Sedbrook JC.** 2004. MAPs in plant cells: delineating microtubule growth dynamics and organization. *Current Opinion in Plant Biology* **7**, 632–640.
- Sheahan MB, Staiger CJ, Rose RJ, McCurdy DW.** 2004. A green fluorescent protein fusion to actin-binding domain 2 of *Arabidopsis* fimbrin highlights new features of a dynamic actin cytoskeleton in live plant cells. *Plant Physiology* **136**, 3968–3978.
- Shibaoka H.** 1994. Plant hormone-induced changes in the orientation of cortical microtubules—alterations in the cross-linking between microtubules and the plasma-membrane. *Annual Review of Plant Physiology and Plant Molecular Biology* **45**, 527–544.
- Sugiyama Y, Wakazaki M, Toyooka K, Fukuda H, Oda Y.** 2017. A novel plasma membrane-anchored protein regulates xylem cell-wall deposition through microtubule-dependent lateral inhibition of Rho GTPase domains. *Current Biology* **27**, 2522–2528.
- Takatani S, Hirayama T, Hashimoto T, Takahashi T, Motose H.** 2015. Abscisic acid induces ectopic outgrowth in epidermal cells through cortical microtubule reorganization in *Arabidopsis thaliana*. *Scientific Reports* **5**, 11364.
- Tsakaya H.** 1995. Developmental genetics of leaf morphogenesis in dicotyledonous plants. *Journal of Plant Research* **108**, 407–416.
- Tsakaya H.** 2002. Leaf development. *The Arabidopsis Book* **1**, e0072.
- Tsakaya H, Tsuge T, Uchimiya H.** 1994. The cotyledon—a superior system for studies of leaf development. *Planta* **195**, 309–312.
- Vanneste S, Friml J.** 2013. Calcium: the missing link in auxin action. *Plants* **2**, 650–675.
- Wang YS, Motes CM, Mohamalawari DR, Blancaflor EB.** 2004. Green fluorescent protein fusions to *Arabidopsis* fimbrin 1 for spatio-temporal imaging of F-actin dynamics in roots. *Cell Motility and the Cytoskeleton* **59**, 79–93.
- Wasteneys GO.** 2002. Microtubule organization in the green kingdom: chaos or self-order? *Journal of Cell Science* **115**, 1345–1354.
- Wasteneys GO, Yang Z.** 2004a. The cytoskeleton becomes multidisciplinary. *Plant Physiology* **136**, 3853–3854.
- Wasteneys GO, Yang Z.** 2004b. New views on the plant cytoskeleton. *Plant Physiology* **136**, 3884–3891.
- Winter D, Vinegar B, Nahal H, Ammar R, Wilson GV, Provart NJ.** 2007. An ‘Electronic Fluorescent Pictograph’ browser for exploring and analyzing large-scale biological data sets. *PLoS One* **2**, e718.
- Wood P.** 1984. Specific interaction of aniline blue with (1,3)-beta-D-glucan. *Carbohydrate Polymers* **4**, 49–72.
- Xiao H, Jiang N, Schaffner E, Stockinger EJ, van der Knaap E.** 2008. A retrotransposon-mediated gene duplication underlies morphological variation of tomato fruit. *Science* **319**, 1527–1530.
- Yang BJ, Wendrich JR, De B, Weijers D, Xue HW.** 2018. OsIQD14 regulates grain shape through modulating the microtubule cytoskeleton. *bioRxiv* doi: 10.1101/275552. [Preprint.]
- Zhang C, Halsey LE, Szymanski DB.** 2011. The development and geometry of shape change in *Arabidopsis thaliana* cotyledon pavement cells. *BMC Plant Biology* **11**, 27.